J Solid State Electrochem (2016) 20:1065–1074
DOI 10.1007/s10008-015-2986-5

ORIGINAL PAPER

Chemical composition and electronic structure of anodic passive films on low-C 13CrNiMo stainless steel

C. A. Gervasi[1,2] · C. M. Méndez[3] · A. E. Bolzán[1] · P. D. Bilmes[2] · C. L. Llorente[2]

Received: 4 May 2015 / Revised: 15 July 2015 / Accepted: 20 July 2015 / Published online: 30 July 2015

Abstract Mott–Schottky analysis and electrochemical and X-ray photoelectron spectroscopy (XPS) measurements were performed on passive films formed on low-C 13CrNiMo stainless steel with different applied heat treatments. Heat treatments render particular microstructural features of the alloy with a significant impact on the ability of the passive films to afford adequate protection against localized corrosion. A lower level of retained austenite in the substrate renders thinner passive films. Phosphates coexist with oxidized Fe(III) compounds as the prevailing species in the anodic layers. Mo was only detected in the oxide film formed on the sample with a higher retained austenite content.

Passive layers behave as *n*-type semiconductors with two types of donors, namely, shallow-level and deep-level states. The observed flat band potential $V_{FB} \cong$ -0.425 ± 0.005 V vs. standard calomel electrode (SCE) is independent of the thermal treatment of the alloy but under potential bias conditions at the corrosion potential the occurrence of the cathodic reaction on the oxide surface is hindered on the sample with higher retained austenite in its microstructure as compared to the sample with lower retained austenite content.

Keywords Alloys · Heat treatment · Stainless steel · Passive films · Corrosion

✉ C. A. Gervasi
gervasi@inifta.unlp.edu.ar

✉ C. M. Méndez
cmendez@fceqyn.unam.edu.ar

A. E. Bolzán
aebolzan@inifta.unlp.edu.ar

[1] Instituto de Investigaciones, Fisicoquímicas Teóricas y Aplicadas (INIFTA), Facultad de Ciencias Exactas, Universidad Nacional de la Plata, CONICET, Sucursal 4-C.C.16, 1900 La Plata, Argentina

[2] Laboratorio de Investigaciones de Metalurgia Física (LIMF), Facultad de Ingeniería, Universidad Nacional de la Plata, Calle 1 y 47, 1900 La Plata, Argentina

[3] Laboratorio de Corrosión, Facultad de Ciencias Exactas, Químicas y Naturales, Universidad Nacional de Misiones, Félix de Azara 1552, 3300 Posadas, Argentina

Introduction

Low-C martensitic stainless steels are increasingly used in the oil and gas industry since these alloys combine good mechanical properties with a satisfactory corrosion resistance. Thus, when corrosive conditions are not particularly severe, the use of these stainless steels becomes quite attractive due to their lower cost, which makes them the natural choice for the replacement of either carbon steels that have a lower corrosion resistance or duplex stainless steel grades having higher prices [1–4].

Appropriate post-weld heat treatments (PWHTs) develop unique microstructural features on low-C martensitic stainless steel (lean, medium or high supermartensitic grades). These distinctive phase transformations and microstructural evolution result in higher amounts of retained austenite at room temperature after reverse transformation of martensite to austenite that, in turn, control some of the properties of the passive layer that can be developed on its surface. Moreover, stability of the passive layer affects the development of localized corrosion processes significantly [5]. For low-C 13CrNiMo stainless steels, a direct correlation was found between pitting susceptibility and volume fraction of retained austenite [6, 7]. A larger amount of retained austenite prevents formation of chromium precipitates preserving higher

chromium contents in solid solution and determining a lower pitting susceptibility. Additionally, thicker and more protective films result [8].

In metal electrodes, charge transfer takes place through electrons with energy near the Fermi level. On the other hand, at a semiconducting passive layer/electrolyte junction, charge transfer proceeds through conduction-band electrons or valence-band holes. This semiconductor/electrolyte interface usually involves a space-charge layer, which largely governs its electrochemical properties, characterized by rectifying behavior and an anodic current, for *n*-type films, which is observed only when minority carriers are created by illuminating the electrode with photons of energy higher than the bandgap. Thus, in order to evaluate the electrochemical properties of this interface, it is essential to determine the position of the band-edge energies on a redox potential scale using the flat band potential V_{FB}.

In a simple theory, the space-charge layer is governed by the difference between the applied electrode potential V and the flat band potential V_{FB}. However, electronic states in the bandgap often alter this simple model, leading to a more complex behavior. Consequently, Mott–Schottky plots are typically used to characterize the energetics of passive films on stainless steel/electrolyte junctions.

Hakiki et al. [9] studied the electronic structure of oxide films thermally grown on 304 stainless steels by using a Mott–Schottky analysis and concluded that an *n*-type semiconductor behavior can be observed in the potential window lying more anodic than −0.5 V standard calomel electrode (SCE). The electronic structure model describes the formation of a Schottky barrier at the semiconductor oxide/electrolyte interface that plays a vital role for the occurrence of electrochemical transformations. The passive current is then related to the level of defects in the oxide [10]. These defects are associated with localized states acting as donor or acceptor species that introduce shallow electronic levels in the bandgap. Furthermore, dopants influence the reactivity of passive interfaces markedly [10]. Several works dealt with the determination of properties of passive films such as the potential of zero charge, the flat band potential, the optical band gap, and the correlation of these parameters with the susceptibility to pitting corrosion [11].

Typical results of the chemical composition analysis of passive films on stainless steels reveal the presence of oxides of chromium, nickel, and iron. The structure of the passive film corresponds typically to an inner region near the metal/film interface, where the chromium oxide Cr_2O_3 predominates and an outer region containing mainly iron oxides, namely Fe_2O_3 [9]. The thickness of the outer layer of Fe_2O_3 increases according to the value of the anodic formation potential. Across the passive film, the Cr/Fe atomic ratio increases from the surface and reaches a peak value near the metal/film interface [9]. Moreover, the composition is also determined by the formation potential of the anodic oxide film, as clearly shown in studies carried out on 316L stainless steel [12].

Different experimental techniques, based on optical and electrochemical measurements, are commonly used to gain insight into essential characteristics of passive films related to the alloy's corrosion resistance, like chemical composition, ionic transport, and electronic properties. In particular, electrochemical impedance spectroscopy has proved to be very useful to achieve this goal [13–15].

We previously characterized, as indicated above, the effect on pitting susceptibility of thermal cycles resulting from PWHTs applied to low-C martensitic stainless steels. This served as a motivation to inquire, for the first time, into the influence that the passive films of these treated stainless steels have on the rate of the electron transfer process necessary to sustain the cathodic reaction coupled to anodic localized processes. Regarding the performance of low-C martensitic stainless steels, Vignal et.al. [3] stated very recently that "there are still open questions concerning the relationships between the specimen microstructure, the passive properties of the alloy and the corrosion mechanisms." This is the knowledge gap we intend to bridge here.

The main objective of this work is to study anodic passive films formed on low-C 13CrNiMo stainless steels that exhibited different microstructures resulting from appropriate heat treatments. Chemical composition and electronic properties of the passive films were evaluated and correlated with pitting corrosion susceptibility.

Experimental methods

Experiments were performed on low-C martensitic stainless steel specimens with weight percentage composition as follows: 0.03%C, 0.6%Mn, 0.3%Si, 12.74%Cr, 3.71%Ni, 0.53%Mo, 0.01%S, 0.008%P, and the remainder Fe.

Different heat treatments were applied to the specimens as shown in Table 1. For both conditions, volume fractions of austenite were measured by X-ray diffraction from a Rietveld analysis. X-ray diffraction patterns were obtained at room temperature with a Philips PW 1710 diffractometer, furnished with diffracted-beam graphite monochromator. Data were collected by using Cu-Kα radiation in the range $10° \leq 2\theta \leq 120°$ at a step interval of 0.02°. Rietveld analysis was performed by using the Fullprof program. Further details can be found elsewhere [7]. According to this analysis, in the microstructure resulting from the application of a double tempering (condition M), higher amounts of retained austenite content resulted (Table 1).

Stainless steel samples were initially ground to a mirror-like finish, and next, they were potentiostatically passivated for 2 h in 0.5 M Na_2HPO_4 solution (pH = 9.2), at 25±1 °C. Electrochemical experiments were performed in a conventional three-electrode cell by using a Zahner IM6e measuring

Table 1 Description of the applied heat treatments

Condition	Heat treatments	Temperature (°C)	Time (h)	Austenite content (vol%)
E	Solution annealing + tempering	950 + 550	1 2	2
M	Solution annealing + double tempering	950 + 670 + 600	1 2 8	22

instrument. The working electrodes had 1 cm^2 geometric surface area. The counter-electrode was a Pt sheet of large surface area. Potentials were measured against a standard calomel electrode (SCE, 0.242 V in the NHE scale). A nitrogen stream was purged through the electrolyte solutions before those experiments where it was required to remove dissolved oxygen. Inert gas circulation was maintained above the solution level during measurements performed in the absence of dissolved oxygen.

In a typical experiment for Mott–Schottky analysis, the applied potential was sequentially stepped from the initial anodic formation potential E_f towards increasingly cathodic potential values. Potential steps had an amplitude of 0.05 V. At each potential, impedance spectra were recorded in the high-frequency region 100 kHz $\geq f \geq$ 1 Hz.

X-ray photoelectron spectroscopy (XPS) was employed to study the composition of the anodic layers. XPS measurements were performed using an ESCA 3 Mark II instrument, with MgK_α X-ray radiation ($h\nu$ = 1253.6 eV) as the excitation source. The composition of the surface regions of the anodic films was determined by XPS analysis followed by argon ion etching for selected intervals of time. Ion etching was accomplished with an Ar^+-ion beam of 3 keV bombardment energy at an incidence angle of 60°.

Low-resolution survey spectra were recorded between binding energies of 0 and 1100 eV. These survey scans were sufficient for the identification of all detectable elements present. Predominantly, the O 1s, Fe 2p, Ni 2p, Cr 2p, and Mo 3d photoelectron lines were observed in these wide range spectra. The carbon contamination C 1s line, due to ubiquitous impurities, was also observed and recorded to monitor the charging. The reproducibility of the binding energy values was within 0.2 eV. High-resolution spectra were also recorded for the above mentioned photoelectron lines at each depth analyzed.

Results and discussion

Potentiodynamic polarization

Potentiodynamic polarization curves for heat-treated samples E and M (Fig. 1) show corrosion potentials at −0.758 and −0.526 V (SCE), respectively, followed by the potential windows for the passive state limited by transpassive current peaks located at a potential close to 0.6 V (SCE). At the anodic end of the scans, increasing currents due to oxygen evolution can be observed. Comparative features in the potentiodynamic responses were discussed in the literature [8] in terms of compositional and structural changes in the surface film.

Mott-Schottky analysis

Bianchi et al. [16] highlighted the importance of the cathodic reaction taking place on the passive film during pitting corrosion. Thus, a kinetically hindered cathodic reaction determines a modification of the corrosion potential associated with the gradual increase in the anodic currents inside the growing pits. This, in turn, affects life and morphology of the pits.

When the electrode impedance at high frequencies departs from a simple series RC circuit model, frequency dispersion limits the validity of the findings. Regarding frequency dispersion of the interfacial capacitance, two types of behavior in Mott–Schottky plots have been described. The first type is associated with both the slopes and the intercepts varying with frequency, and the second type is related to frequency-dependent slopes but all the lines converging to a single intercept on the potential axis.

To take into account frequency dispersion of the interfacial capacitance C, the latter was calculated by using Brug's expression [17] given in equation (1). This equation corresponds to a surface distribution of the differential capacitance according to the applicability of an equivalent circuit consisting of the electrolyte resistance R_Ω connected in series with an impedance element resulting from the parallel connection of a constant phase element CPE and the polarization resistance R_{CT}. The impedance of a CPE has the form given in equation (2) where

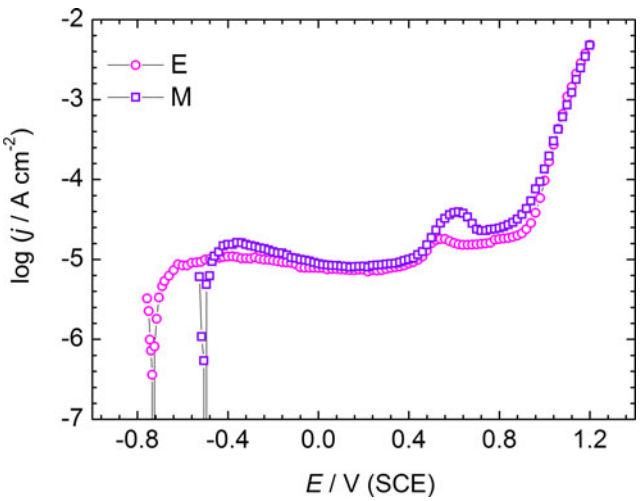

Fig. 1 Potentiodynamic polarization curves for low-C 13CrNiMo stainless steels thermally treated as indicated in Table 1. Data taken form Ref. [8]

$j = \sqrt{-1}$, $\omega = 2\,\pi\,f$ is the AC signal frequency, and when the coefficient n equals 1, a CPE simplifies to a capacitor.

$$C = \left[\frac{Y_o}{\left[R_\Omega^{-1} + R_{CT}^{-1}\right]^{1-n}}\right]^{\frac{1}{n}} \quad (1)$$

$$Z_{CPE} = (j\omega)^{-n}/Y_o \quad (2)$$

Strictly speaking, the system's interface corresponding to the sample immersed in the aqueous electrolyte and covered by a passive film exhibits a capacitance C made up of two individual components connected in series: the space-charge capacitance C_{SC} and the Helmholtz capacitance C_H. Since C_{SC} is much smaller than C_H, the value of C is approximately equal to C_{SC}.

The influence of the applied electrode potential V on the space-charge capacitance under depletion conditions can be evaluated from a Mott–Schottky linear plot (C_{SC}^{-2} vs. V), which for an n-type semiconductor is described by equation (3)

$$\frac{1}{C_{SC}^2} = \frac{2}{\varepsilon\varepsilon_0 e N_D}\left(V - V_{FB} - \frac{kT}{e}\right) \quad (3)$$

where N_D is the donor density, ε is the dielectric constant of the film (=12 [18]), $\varepsilon_0 = 8.85 \times 10^{-14}$ F cm^{-1} is the vacuum permittivity, $e = 1.6 \times 10^{-19}$ C is the electron charge, k is the Boltzmann constant, and T is the absolute temperature. As usual, the term kT/e can be considered negligible, V_{FB} can be obtained by extrapolating the linear portion of the plot to $C_{SC}^{-2} = 0$ and N_D can be calculated from its slope.

Figure 2 displays Mott–Schottky (MS) plots for samples E and M that were passivated at $E_f = 0.55$ V (SCE) for 2 h in 0.5 M Na_2HPO_4 solution (pH 9.2). C values were calculated by using Brug's equation, as explained above.

A closer inspection of Fig. 2 reveals the following aspects:

i. Linear MS plots confirm semiconducting behavior of the passive layers within the studied potential range.
ii. Two potential windows can be observed for both samples that are related to two different slopes of the linear MS plots. The more anodic potential window is associated with a smaller slope. This is in agreement with data presented for anodic passive layers on type 316L stainless steel [18]. Positive slopes indicate n-type semiconduction, as the one usually found for an outer part of a surface layer consisting of oxidized Fe species, like Fe_2O_3 and/or FeOOH. These observations are consistent with point defects corresponding to metal interstitials or oxygen vacancies, or both. No evidence for p-type behavior was obtained, indicating that cation vacancies do not have a significant population density in the film compared with the donors species, as reported for passive films on Fe and Fe-Cr alloys in alkaline borate buffers [10, 19],
iii. The observed $V_{FB} \cong -0.425 \pm 0.005$ V (SCE) results independent of the thermal treatment of the alloy. Moreover, this value is in good agreement with reported data for passive films on stainless steel grades 304L and 316L measured in borate buffers with comparable pH [18, 20],
iv. The electronic defect structure corresponds to the presence of two types of donor centers, one being completely ionized at flat band conditions (density N_D) and the second one completely filled (density N_D'). The second slope of the MS plots for larger anodic potentials is inversely proportional to the sum ($N_D + N_D'$). From the two straight portions of the MS plots, N_D and N_D' donor densities were determined for both approaches used to calculate the interfacial capacitance. Results are assembled in Table 2. Large values for the densities of shallow-level donors, N_D, and localized states situated deeper in the bandgap, N_D', were obtained, but still within the typical range for highly disordered and non-stoichiometric passive layers on stainless steels [10].

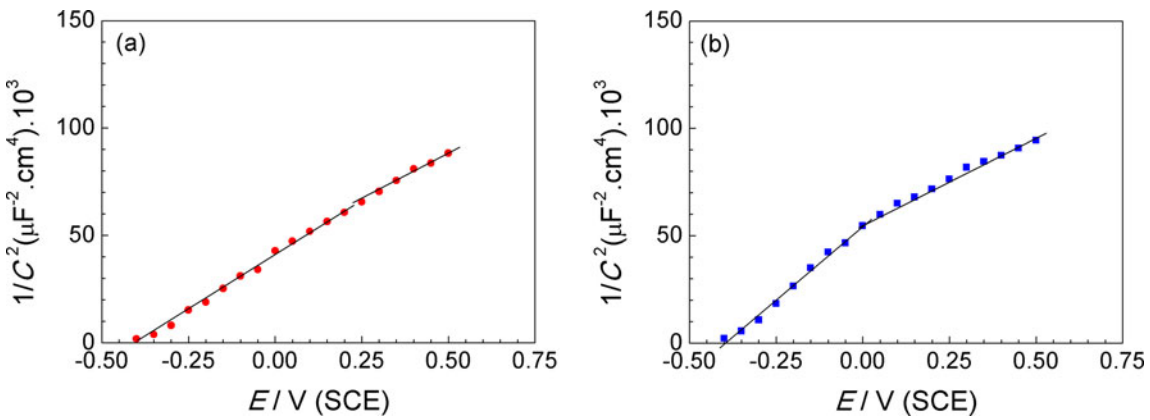

Fig. 2 Mott–Schottky (MS) plots for samples E (**a**) and M (**b**) derived from C values calculated by using Brug's equation (1). Samples were anodically passivated for 2 h in 0.5 M Na_2HPO_4 solution (pH 9.2) at $E_f = 0.55$ V (SCE)

Table 2 Densities for shallow-level and deep-level donor states N_D and N_D', respectively, as derived from MS plots for passive layers anodically grown on samples E and M at a formation potential of 0.55 V (SCE) for 2 h

	V_{FB} ± 5.5 (mV/SCE)	$10^{19}N_D$ (cm^{-3})	$10^{19}N_D'$ (cm^{-3})
Sample E	−425.5	11.47	0.41
Sample M	−425.5	8.56	1.79

A passive film that exhibits a larger donor density N_D, compared with another film obtained under different working conditions, was considered to be less resistant to pitting corrosion when pit nucleation results from an accumulation of point defects [21]. This could explain, to some extent, why sample E is more susceptible to pitting than sample M [8]. Anyhow, it has already been established that there exists a correlation between the distribution of localized states in the passive film, i.e., its defect structure, and the stability of the film [22]. In Table 2, N_D values are larger for sample E as compared with sample M and also larger than N_D' values for each sample.

Polarization measurements and energetics of the interface

The potential scans recorded in the cathodic direction, and shown in Fig. 3, are characterized by a threshold potential beyond which increasingly larger cathodic currents are detected. This feature corresponds to a rectifying behavior in the presence of an energy barrier in a depletion layer of an *n*-type semiconductor/solution junction and validates the method used to calculate V_{FB} in the system [23]. Moreover, Fig. 4 displays the corrosion potentials V_{corr} of samples E and M measured in the Na_2HPO_4 solution under both conditions, specifically, with and without dissolved oxygen. The differences (V_{corr}−V_{FB}) measured in both electrolytes are larger for sample E as compared with sample M and therefore, the passive film on sample E might exhibit less tendency to inhibit the oxygen reduction reaction. It has been claimed that one consequence of the disruption of the oxide films, due to pitting initiation and their repassivation, is a large transient shift in voltage across the interface that results from slow reduction-coupled reactions. Prolonged exposure to cathodic potentials that are caused by electrochemical interactions of the interface might result in altered corrosion resistance of the oxide-film covered surface [24]. Thus, these results are consistent with the previously measured repassivation capability which is different for both samples E and M [8].

Figure 5a displays the energy band diagram of the system at the flat band condition with an energy gap E_g = 2 eV [25] between the conduction band (CB) edge and the valence band (VB) edge. The same diagram is shown in Fig. 5b for an applied cathodic bias that results in the formation of an accumulation layer of electrons at the oxide-electrolyte interface. The Fermi level (E_F) penetrates into the conduction band at the surface. On the potential scale, in V (NHE), the Fermi levels of the redox couples for the aqueous electrolyte decomposition are shown together with the corrosion potentials for both samples E and M. This simple model used to interpret MS plots is based on the assumed presence of a uniform, single-layer passive film, even though the passive film consists most likely of a two-layer structure, as will be shown in relation to XPS measurements.

A higher availability of electrons for the electroreduction reaction at the corrosion potential is observed for sample E as compared with sample M (Fig. 5). It has been shown unequivocally that deep donor states situated in the space-charge region of passive films formed on Fe-Cr-Mo stainless steels are

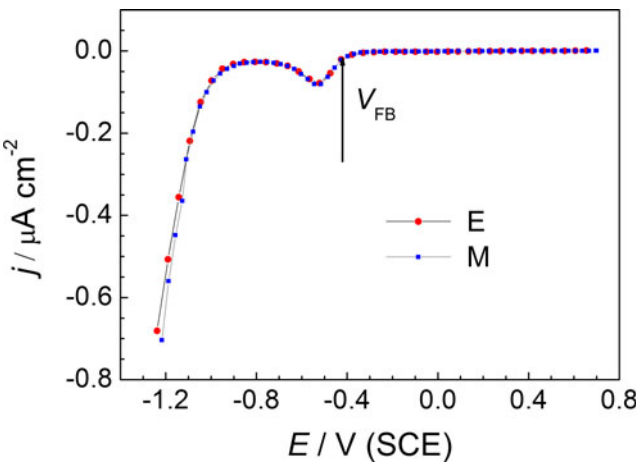

Fig. 3 Cathodic potentiodynamic scans recorded at 10 mVs^{-1} in aerated 0.5 M Na_2HPO_4 solution (pH 9.2)

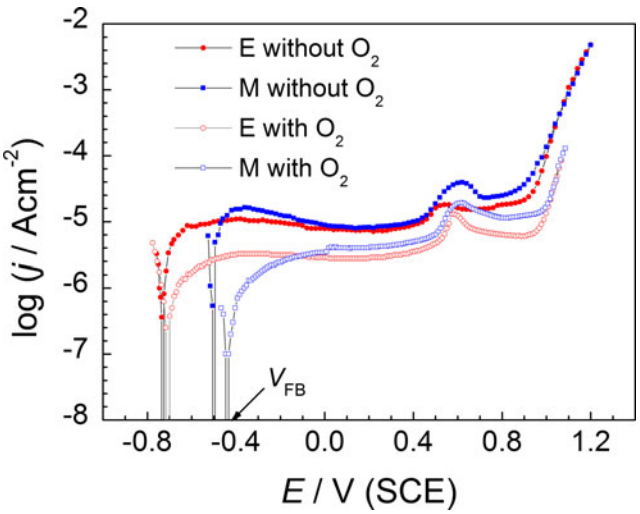

Fig. 4 Potentiodynamic polarization curves recorded by using anodic scans at 1 mV s^{-1} with and without dissolved oxygen in the Na_2HPO_4 solution

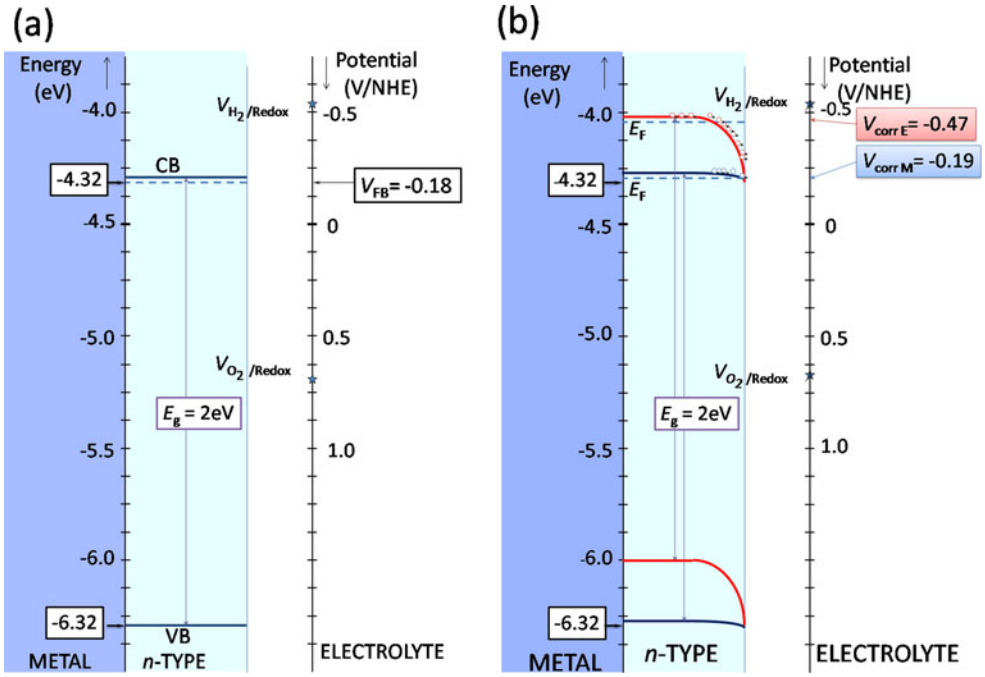

Fig. 5 Energy band diagrams in terms of both electron energy and potential scales, at flat band condition (**a**) and for a cathodic applied potential bias leading to the formation of an accumulation layer (**b**). Positive electron energy is plotted "upward" and positive voltage is plotted "downward." See text for definitions of specific values of energy/potential levels indicated in the graph

responsible for a capacitance behavior which is similar to that displayed in Fig. 2 [25].

X-ray photoelectron spectroscopy measurements

XPS depth profiles recorded on passive layers anodically formed for 2 h at 0.55 V (SCE) on samples E and M revealed the presence of surface species of Ni, Mo, Fe, and Cr distributed throughout the entire film thickness [26–29].

Elemental composition within the surface layers at fixed intervals of sputtering time are shown in Fig. 6a, b for samples E and M, respectively.

As shown in Fig. 6, the oxygen signal detected after 60 min sputtering time becomes considerably reduced for sample E, while for sample M it still maintains a large percentage. This indicates the presence of a comparatively thinner oxide on sample E. Moreover, for sample E contamination and incorporation of species from the electrolyte is clearly more extensive at every sputtering time, what may be due to a higher porosity of its surface film. For sample M, the oxide/metal interfacial region was not reached even after 60 min sputtering time. Although the Cr content of the film increases with sputtering time while the sputtering zone does not reach the metal, the Cr/Fe ratio clearly decreases. The presence of Mo in the oxide film was only detected for sample M. Due to the small percentage of Mo in the alloy, detection of its presence in the surface films cannot be clearly shown for the corresponding concentration scales in Fig. 6. The Ni signal intensity was somewhat stronger in sample M as compared with sample E. The presence of Ni within the surface layers was also detected associated with the presence of $NiCr_2O_4$ in the high-resolution spectra for the Cr 2p3/2 photoelectron line (see Fig. 9 below).

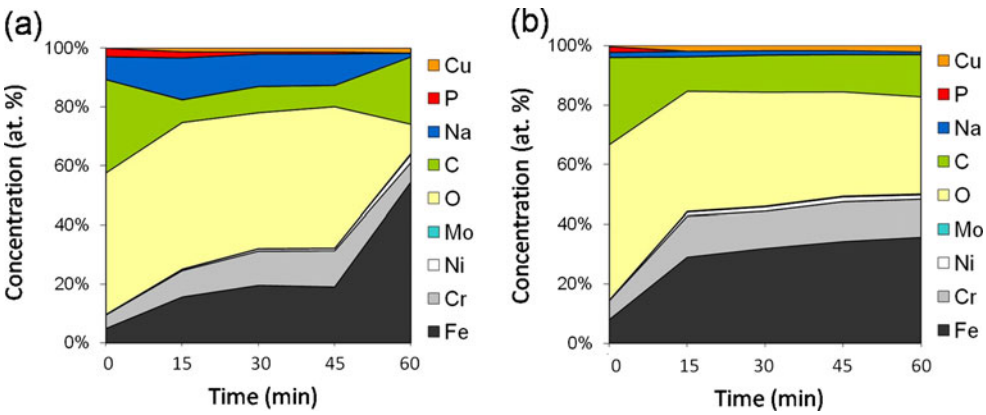

Fig. 6 Sputter depth profiles recorded on anodic surface layers for samples E (**a**) and M (**b**)

At this point, it is worth mentioning that during depth profiling, surface and interface roughening may occur. This, in turn, may cause profiles with broad slopes at the end of plateaus marking oxide phase limits even though the real profile might be sharp [30].

High-resolution spectra for O 1s, Cr $2p_{3/2}$, Fe $2p_{3/2}$, P $2p_{3/2}$, Mo $3d_{5/2}$ y $3d_{3/2}$, Ni $2p_{3/2}$, Na 1s, and C 1s were collected and the different chemical states were identified based on their binding energy values. Since the C signal results from sources other than the metal and the passive layer, it was excluded from the subsequent analysis. Table 3 shows a listing of binding energy values calculated in this study together with values reported in the literature. The signals were deconvoluted into the elementary states of the species through fitting of the high-

Table 3 Binding energy (eV) of the chemical states of elements identified by XPS

Cr $2p_{3/2}$	Cr	Cr_2O_3	$Cr(OH)_3$	CrO_3	$FeCr_2O_4$	$NiCr_2O_4$	
	574.4	576.4	577.4	578.4	575.9	575.2	This study
	574.3	576.8	577.3	578.3			[12]
	574.5	576.4					[31]
		575.3	577.0	578.2			[29]
	574	577.6 578.6	576.4	580.1			[32]
	574.2	575.7	577.3	579.5	575.9	575.2	[33]
	574.5	576.1	577.5				[27]
Fe $2p_{3/2}$	Fe	Fe_3O_4	FeO	Fe_2O_3	FeOOH	$FePO_4$	
	707	707.9	709.1	710.7	711.7	712.4	This study
	706.7	708.2	709.4	710.9	711.8		[12]
	707.2 720.3					712.1	[34]
	707.1		709.2	711.1			[31]
	706.6		709.2	710.7			[29]
	719.92	706.82	707	708.7	724.97		[32]
	707		709.5	711	712		[27]
	706.6		708.4	709.8			[33]
P $2p_{3/2}$	P	$NaPO_3$	$FePO_4.4H_2O$				
	–	134.4	133.4				This study
	129.6	134.1					[34]
	134		133.5				[35]
	133		130.6				
Mo $3d_{5/2}$	Mo	$Fe_2(MoO_4)_3$	MoO_3	MoO_2			
	228.3	232.5	234				This study
			235	232.7			[29]
	227.9	232.5	232.6				[12]
	227.75		232.5				[27]
Ni $2p_{3/2}$	Ni	NiO	$Ni(OH)_2$				
	852.9	853.7	854.7				This study
	852.7	853.8	855.6				[12]
	852.8	854	856.5				[32]
	853						[27]
	852.6	853.7 855.4	854.9 855.7				[33]
Na 1s	Na						
	1072.7						This study
	1072						[31]
O 1s	O^{-2}	OH^-	H_2O	P-containing species			
	530.4	531.4	532.4	530.5			This study
	530.2	531.5	532.5	531.1			[35]
	530.3	531.5					[31]

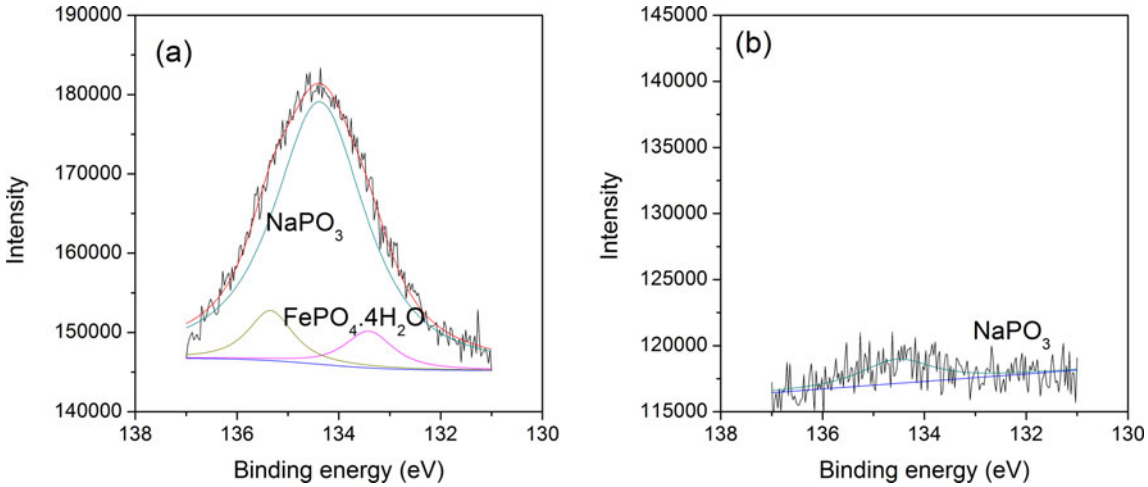

Fig. 7 P $2p_{3/2}$ spectra for sample E (**a**) and M (**b**) recorded after 15 min sputtering time

resolution spectra using components having mixed 70–80 % Gaussian–Lorentzian character. A Shirley background for asymmetric line shapes was employed for all spectra.

The XPS spectrum of O 1s electron binding energy region consists of three peaks originating from O^{-2}, hydroxide or hydroxyl groups, OH^-, and adsorbed water, H_2O (Table 3).

The presence of P in compounds where it is chemically bonded with O was detected in the high-resolution spectra of surface layers treated with up to 15 min sputtering time for sample M (Fig. 7b). The P $2p_{3/2}$ spectra could still be resolved after 45 min sputtering time for sample E where the additional presence of P in $FePO_4.4H_2O$ is detected (Fig. 7a).

For sample E, the high-resolution Fe $2p_{3/2}$ spectra up to 15 min sputtering time exhibits a peak that can be assigned to $FePO_4.2H_2O$, in agreement with data presented in connection with the P $2p_{3/2}$ spectra (Fig. 8a). Moreover, phosphates coexist with oxidized Fe(III) compounds, notably the oxyhydroxide form FeOOH and Fe_2O_3. Fit results of the high-resolution spectra in the region of Fe $2p_{3/2}$ reveal that in the anodic layers of sample M, the most oxidized form Fe_2O_3 is the prevailing species at the surface, while for sputtering times of 15 min or larger the dominating species is Fe_3O_4. The global composition remains practically unaltered for increasing sputtering times beyond 15 min (Fig. 8b). In the passive film formed in phosphate buffer, pH 8.4, a significant amount of phosphates was reported to be present in the outer part of the film [35]. Moreover, bands related to Fe_3O_4 and FeOOH species were obtained by using Laser Raman Spectroscopy, on films formed in phosphate solutions pH 8.7 and working with Fe electrodes [36, 37, and references therein].

Peaks assignment for the high-resolution Cr $2p_{3/2}$ spectra recorded for sample E, for sputtering times varying from 15 min to 30 min, indicates that $Cr(OH)_3$ is the prevailing species in that portion of the surface film (Fig. 9b). Intensities of the spectra for sputtering times between 15 and 45 min are larger than the intensity of the corresponding spectrum recorded at the surface. Binding energy peaks in the Cr $2p_{3/2}$ spectra recorded for sample M can be attributed to the presence of $Cr(OH)_3$ as the prevailing species and also to a compound containing Ni ($NiCr_2O_4$), which in sample E was not detected (Fig. 9b).

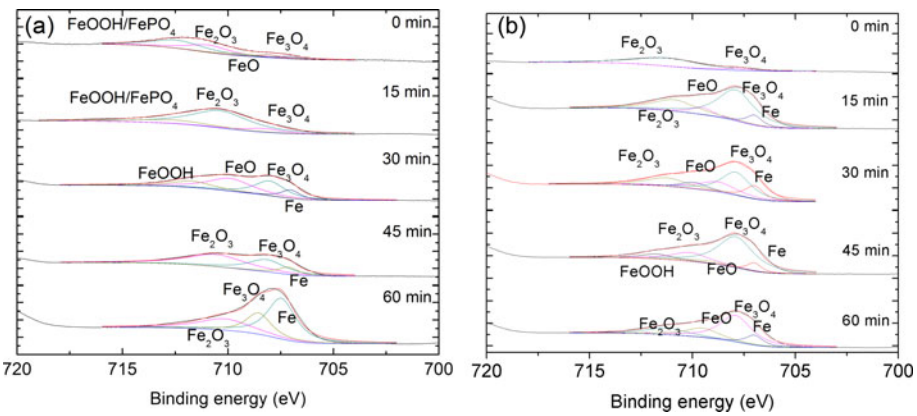

Fig. 8 Fe $2p_{3/2}$spectra for samples E (**a**) and M (**b**) with different sputtering times

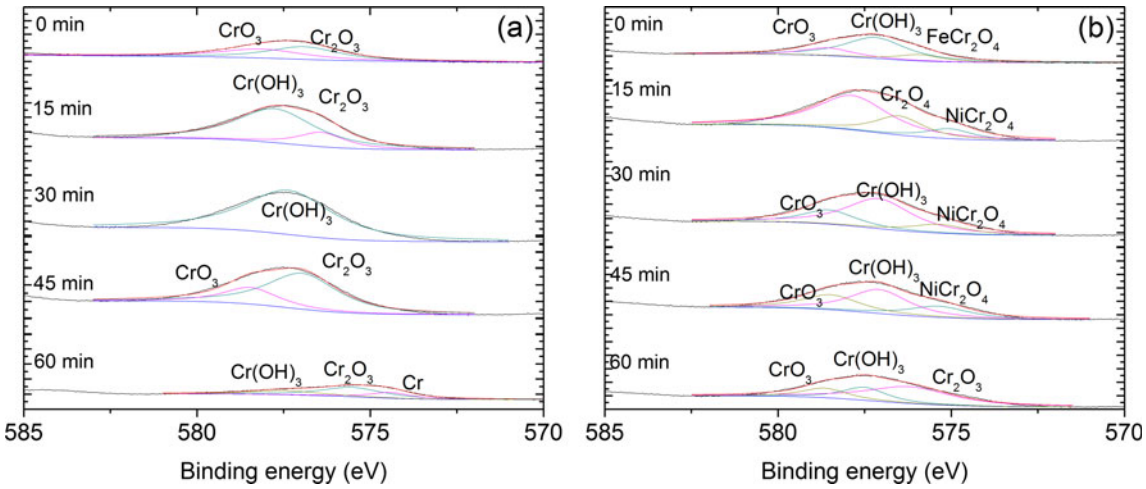

Fig. 9 $Cr2p_{3/2}$spectra for samples E (**a**) and M (**b**) with different sputtering times

Conclusions

Thickness, chemical composition, and electronic conduction are the properties of the passive films formed on low-C 13CrNiMo stainless steels that clearly depend on the heat treatments applied to the base alloys. The applied heat treatments, in turn, modify the microstructural features of the stainless steels. Thus, microstructures characterized by a high content of retained austenite yield more protective properties of the passive layers that can be correlated with higher corrosion resistance, namely, hindered kinetics of the cathodic reduction reaction, lower point defects concentration, thicker films, and a composition rendering more stable passive layers.

A lower level of retained austenite in the substrate renders thinner passive films.

The chemical composition is consistent with the presence of phosphates that coexist with oxidized Fe(III) compounds. Mo was detected only in the oxide film formed on the sample with higher retained austenite content.

The electronic defect structures correspond to *n*-type semiconductors containing two types of donor centers, one being completely ionized at flat band conditions and the second one being completely filled. The observed flat band potential $V_{FB} \cong -0.425 \pm 0.005$ V (SCE) is independent of the thermal treatment of the alloy. However, at the corrosion potential, V_{FB} is related to a less favorable condition for the occurrence of the cathodic reaction, on the oxide surface of the sample with higher retained austenite in its microstructure.

Acknowledgments This work was financially supported by Agencia Nacional de Promoción Científica y Tecnológica of Argentina (ANPCYT, PICT 2013-0387), Consejo Nacional de Investigaciones Científicas y Técnicas (CONICET) and Comisión de Investigaciones Científicas de la Provincia de Buenos Aires (CICPBA). CLL, AEB, and CAG are researchers at CICPBA.

References

1. Mesquita TJ, Chauveau E, Mantel M, Bouvier N, Koschel D (2014) Corrosion and metallurgical investigation of two supermartensitic stainless steels for oil and gas environments. Corros Sci 81:152–161
2. Della Rovere CA, Aquino JM, Ribeiro CR, Silva R, Alcântara NG, Kuri SE (2015) Corrosion behavior of radial friction welded supermartensitic stainless steel pipes. Mater Des 65:318–327
3. Vignal V, Ringeval S, Thiébaut S, Tabalaiev K, Dessolin C, Heintz O, Herbst F, Chassagnon R (2014) Influence of the microstructure on the corrosion behaviour of low-carbon martensitic stainless steel after tempering treatment. Corros Sci 85:42–51
4. Xu D, Liu Y, Ma Z, Li H, Yan Z (2014) Structural refinement of 00Cr13Ni5Mo2 supermartensitic stainless steel during single-stage intercritical tempering. Int J Min Metall Mater 21:279–288
5. Schmuki P, Böhni H (1995) Illumination effects on the stability of the passive film on iron. Electrochim Acta 40:775–783
6. Gervasi CA, Bilmes PD, Llorente CL (2007) In: Wang IS (ed) Corrosion research trends. New York, Nova Science Publishers
7. Bilmes PD, Llorente CL, Méndez CM, Gervasi CA (2009) Microstructure, heat treatment and pitting corrosion of 13CrNiMo plate and weld metals. Corros Sci 51:876–881
8. Gervasi CA, Méndez CM, Bilmes PD, Llorente CL (2011) Analysis of the impact of alloy microstructural properties on passive films formed on low-C 13CrNiMo martensitic stainless steels. Mater Chem Phys 126:178–182
9. Hakiki NE, Montemor MF, Ferreira MGS, da Cunha BM (2000) Semiconducting properties of thermally grown oxide films on AISI 304 stainless steel. Corros Sci 42:87–702
10. Gaben F, Vuillemin B, Oltra R (2004) Influence of the chemical composition and electronic structure of passive films grown on 316L SS on their transient electrochemical behavior. J Electrochem Soc 151:B595–B604
11. Szklarska-Smialowska Z (2002) In: Frankel GS, Isaacs HS, Scully JR, Sinclair JD (eds) Corrosion science: a retrospective and current status in honor of Rober P. Frankenthal. The Electrochemical society, New Jersey 251:265
12. Feng Z, Cheng X, Dong C, Xu L, Li X (2010) Passivity of 316L stainless steel in borate buffer solution studied by Mott–Schottky analysis, atomic absorption spectrometry and X-ray photoelectron spectroscopy. Corros Sci 52:3646–3653
13. Castro EB (1994) Analysis of the impedance response of passive iron. Electrochim Acta 39:2117–2123

14. Macdonald DD, Smedley SI (1990) An electrochemical impedance analysis of passive films on nickel(111) in phosphate buffer solutions. Electrochim Acta 35:1949–1956
15. Lai WY, Zhao WZ, Yin ZF, Zhang J (2012) EIS and XPS studies on passive film of AISI 304 stainless steel in dilute sulfuric acid solution. Surf Interf Anal 44:418–425
16. Bianchi G, Cerquetti A, Mazza F, Torchio S (1970) Chemical etching and pitting of stainless steel. Corros Sci 10:19–27
17. Brug GJ, Van Den Eeden ALG, Sluyters-Rehbach M, Sluyters JH (1984) The analysis of electrode impedances complicated by the presence of a constant phase element. J Electroanal Chem 176:275–295
18. Nicic I, Macdonald DD (2008) The passivity of type 316L stainless steel in borate buffer solution. J Nuc Mat 379:54–58
19. Tsuchiya H, Fujimoto S, Shibata T (2004) Semiconductive properties of passive films formed on Fe-18Cr in borate buffer solution. J Electrochem Soc 151:B39
20. Hamadou L, Kadri A, Benbrahim N (2010) Impedance investigation of thermally formed oxide films on AISI 304L stainless steel. Corros Sci 52:859–864
21. Amri J, Souier T, Malki B, Baroux B (2008) Effect of the final annealing of cold rolled stainless steels sheets on the electronic properties and pit nucleation resistance of passive films. Corros Sci 50:431–435
22. Schmuki P, Bohni H (1992) Metastable pitting and semiconductive properties of. J Electrochem Soc 139:1908–1913
23. Harrington SP, Devine TM (2009) The influence of the semiconducting properties of passive films on localized corrosion rates. ECS Trans 16:117–123
24. Gilbert JL, Mali SA (2012) In: Eliaz N (ed) Degradation of implant materials. New York, Springer
25. Hakiki NE (1996) Electronic structure of passive films formed on molybdenum-containing ferritic stainless steels. J Electrochem Soc 143:3088–3094
26. Hakiki NE, Boudin S, Rondot B, Da Cunha BM (1995) The electronic structure of passive films formed on stainless steels. Corros Sci 37:1809–1822
27. Kocijan A, Donik Č, Jenko M (2007) Electrochemical and XPS studies of the passive film formed on stainless steels in borate buffer and chloride solutions. Corros Sci 49:2083–2098
28. Montemor MF, Simoes AMP, Ferreira MGS, Da Cunha BM (1999) The role of Mo in the chemical composition and semiconductive behaviour of oxide films formed on stainless steels. Corros Sci 41: 17–34
29. Zou D, Liu R, Li J, Zhang W, Wang D, Han Y (2014) Corrosion resistance and semiconducting properties of passive films formed on 00Cr13Ni5Mo2 supermartensitic stainless steel in Cl^- environment. J Iron Steel Res Int 21:630–636
30. Strehblow H-H, Marcus P (2006) In: Marcus P, Mansfeld F (eds) Analytical methods in corrosion science and engineering. Boca Raton, CRC Press
31. Vayer M, Reynaud I, Erre R (2000) XPS characterisations of passive films formed on martensitic stainless steel: qualitative and quantitative investigations. J Mat Sci 35:2581–2587
32. Natarajan R, Palaniswamy N, Natesan M, Muralidharan V.S. (2009) XPS analysis of passive film on stainless steel. Open Corros J 2:114–124
33. Biesinger MC, Payne BD, Grosvenor AP, Lau LWM, Gerson AR, Smart RSC (2011) Resolving surface chemical states in XPS analysis of first row transition metals, oxides and hydroxides: Cr, Mn, Fe, Co and Ni. Appl Surf Sci 257:2717–2730
34. Jiang H, Wang J, Ding B (1992) Surface characterization of Ni64P20Fe16 amorphous alloy by X-ray photoelectron spectroscopy and auger electron spectroscopy. Ch J Met Sci Tech 8:157–162
35. Sieber IV, Hildebrand H, Virtanen S, Schmuki P (2006) Investigations on the passivity of iron in borate and phosphate buffers, pH 8.4. Corros Sci 48:3472–3488
36. Giacomelli C, Giacomelli FC, Bortolluzzi RL, Spinelli A (2006) Properties of potentiostatic passive films grown on iron electrodes immersed in weak-alkaline phosphate solutions. Anti-Corros Meth Mat 53:232–239
37. Giacomelli C, Spinelli A (2004) A potentiodynamic and SEM study of the behaviour of iron in pH 8.9-11.0 phosphate solutions. Anti-Corros Meth Mat 51:189–199